Constraints on absolute chamber volume from geodetic measurements: Trapdoor faulting in the Galapagos

Yujie Zheng[1], Laura A Blackstone[2], and Paul Segall[2]

[1]California Institute of Technology
[2]Stanford University

November 26, 2022

Abstract

Magma chamber volume is critical for volcano monitoring and forecasting. Standard geodetic methods cannot constrain the total volume, only the change in volume. Here, we show that stress perturbations associated with trapdoor faulting allow bounds to be placed on the total chamber volume at Sierra Negra volcano, in the Galapagos. The deformation response of the magma chamber to faulting depends on both the absolute chamber volume and the compressibility of the magma. Bubble-free magma provides the lower limit on compressibility, thus an upper bound on the chamber volume of 13.6 to 20.6 km^3, depending on fault dip. We estimate an upper limit on compressibility using a conduit model relating volatile content to lava fountain height, which is compared with observations from the 2005 eruption, constrained by volatile content of olivine melt inclusions. This yields a lower bound on chamber volume of 0.5 times the upper bound.

Constraints on absolute chamber volume from geodetic measurements: Trapdoor faulting in the Galapagos

Yujie Zheng[1], **Laura Blackstone**[2], **Paul Segall**[2]

[1]Division of Geological and Planetary Sciences, California Institute of Technology
[2]Geophysics Department, Stanford University

Key Points:

- The best fitting trapdoor faults are near vertical and dip steeply to the north (88 degree).
- An upper bound on chamber volume is between 13.6 km^3 and 20.6 km^3, depending on fault dip.
- The lower bound on volume is one-half the upper bound.

Corresponding author: =name=, `=email address=`

Abstract

Magma chamber volume is critical for volcano monitoring and forecasting. Standard geodetic methods cannot constrain the total volume, only the change in volume. Here, we show that stress perturbations associated with trapdoor faulting allow for bounds to be placed on the total chamber volume at Sierra Negra volcano, in the Galapagos. The deformation response of the magma chamber to faulting depends on both the absolute chamber volume and the compressibility of the magma. Bubble-free magma provides the lower limit on compressibility, thus an upper bound on the chamber volume of 13.6 to 20.6 km^3, depending on fault dip. We estimate an upper limit on compressibility using a conduit model relating volatile content to lava fountain height, which is compared with observations from the 2005 eruption, constrained by volatile content of olivine melt inclusions. This yields a lower bound on chamber volume of 0.5$\times$ the upper bound.

Plain Language Summary

It is important to understand the size of subterranean magma reservoirs since the volume of available magma bounds the size of short-lived eruptions. In this study, we analyze unique trapdoor faulting earthquakes observed at the Sierra Negra volcano. These events last only a few seconds and cause unique displacements of the ground surface. The volume change and magma pressure drop due to trapdoor faulting depend on the product of chamber volume and magma compressibility. The lower limit of the compressibility is for bubble-free magma. We estimate an upper bound by using observations of "fire fountain" heights during the 2005 eruption. Higher gas content, and thus more compressible magma, lead to higher fire fountains. We find an upper bound on the magma volume of 13.6 km^3 to 20.6 km^3, depending on fault dip. We also find that the observed fire fountain height can be fit with plausible H_2O content and up to 0.15 weight % CO_2, which leads to a lower bound of magma volume of one-half the upper bound. Our results will be an important benchmark for comparison with other methods of estimating magma chamber volume and form a useful constraint for other similar volcanoes worldwide.

1 Introduction

The volume of magma reservoirs is critical for volcano monitoring and forecasting. The total volume provides an upper bound on the possible eruptive volume, assuming no recharge during the eruption. Knowledge of subsurface magma volumes also helps constrain models of magma chamber evolution. However, determining the total chamber volume from geophysical methods has been challenging. Seismic tomography can map the distribution of wave speeds and attenuation, but employing these results to estimate volumes of melt is not straightforward (Lees, 2007; Paulatto et al., 2012; Rawlinson et al., 2014). The same is true for electromagnetic imaging. The distribution of earthquake hypocenters can provide a qualitative sense of magma chamber volume, but location uncertainty and the potential for hot, aseismic rock surrounding magma reservoirs limit quantitative analysis. Geochemical mixing models can provide estimates of the volume of the well-mixed portion of shallow reservoirs (D. Geist et al., 2002; Pietruszka & Garcia, 1999).

Standard geodetic models constrain the *change* in chamber volume but place weak if any constraints on total chamber volume (Segall, 2013). This is well expressed, for example, in the "Mogi model" (Yamakawa, 1955; Mogi, 1958), in which the amplitude of surface deformation is proportional to the product of the pressure change Δp and the total volume V, and inversely proportional to the shear modulus $\Delta p V/\mu$.

The absolute chamber volume can be inferred from geodetic observations if there are independent constraints on pressure change. Such analyses have been conducted at Kīlauea volcano, where active lava lakes were hydraulically connected to the summit chamber, such that changes in lava level can be interpreted as changes in chamber pressure (Johnson, 1992; Denlinger, 1997; Segall et al., 2001; Anderson et al., 2015). Estimates using this approach range from 240 km^3 for the entire magmatic system, including the rift zones (Denlinger, 1997), to 20 km^3 for the summit chamber (Segall et al., 2001), to as low as ~ 1 km^3 for the shallow Halema'uma'u source of episodic deflation-inflation events (Anderson et al., 2015). Most recently, Anderson et al. (2019) combined the remarkable drainage of the summit lava lake during the early stage of the 2018 eruption with Global Positioning System (GPS), tilt, and Interferometric Synthetic Aperture Radar (InSAR) data to constrain the volume of the summit Halema'uma'u reservoir to between 2.5 to 7.2 km^3 at 68% confidence bounds. This work shows that it is possible to determine the total magma chamber volume even without open conduits from the chamber to the surface. In particular, we show that perturbations in stress associated with trapdoor faulting events allow bounds to be placed on the total volume of the magma chamber at Sierra Negra volcano in the Galapagos.

Sierra Negra is the largest and the most voluminous of the six actively deforming volcanoes in the western Galapagos islands, with the most recent eruption in 2018 (Vasconez et al., 2018; Bell et al., 2021). Inflation at Sierra Negra has been punctuated by several trapdoor faulting events, with slip occurring along a complex set of intra-caldera faults with outward dipping fault scarps (Figure 1) along the southern and western margin of the caldera (Reynolds et al., 1995). The first indication of trapdoor faulting came from InSAR observations spanning 1997-98 and is thought to be associated with a M_w 5.0 event on 11 January 1998 (Amelung et al., 2000; Jónsson et al., 2005). A second trapdoor faulting event, associated with a m_b 4.6 earthquake was well captured by both InSAR and GPS data on 16 April 2005 (Chadwick et al., 2006; Jónsson, 2009). The GPS station GV06 was uplifted by almost one meter within 10 seconds during this event. In comparison, the prior inflation rate at Sierra Negra was approximately 0.1 cm/day (Chadwick et al., 2006). The short duration implies that negligible amounts of magma left or entered the chamber during the faulting event. Both the 2005 and the 2018 eruptions were also preceded by trapdoor faulting events (Chadwick et al., 2006; S.-H. Yun, 2007; Vasconez et al., 2018), suggesting they influenced the subsequent eruptions.

Here we analyze both GPS and InSAR data for the trapdoor faulting event on 16 April 2005. The mechanical response of the magma chamber to the trapdoor faulting depends on the product of the total chamber volume and magma compressibility and is clearly expressed in the surface deformation. We show that by constraining the relative compressibility of the magma and the magma chamber it is possible to constrain the absolute volume of the shallow magma reservoir.

2 Method

This section presents a 3D fault-chamber model in an elastic half space to demonstrate the interaction between trapdoor faulting and the magma chamber. Before a trapdoor event, magma influx leads to increased pressure and inflationary deformation without fault slip. During the trapdoor event the fault slips while the mass of magma within the chamber remains unchanged. Magma migrates within the reservoir on the time scale of the faulting event to eliminate pressure gradients generated by the sudden fault slip.

Models of Sierra Negra based on GPS and InSAR data have indicated a sill-like chamber with its top at a depth of about 2 km, though a diapir with a flat top also provides an adequate fit (S. Yun et al., 2006; Amelung et al., 2000; Chadwick et al., 2006).

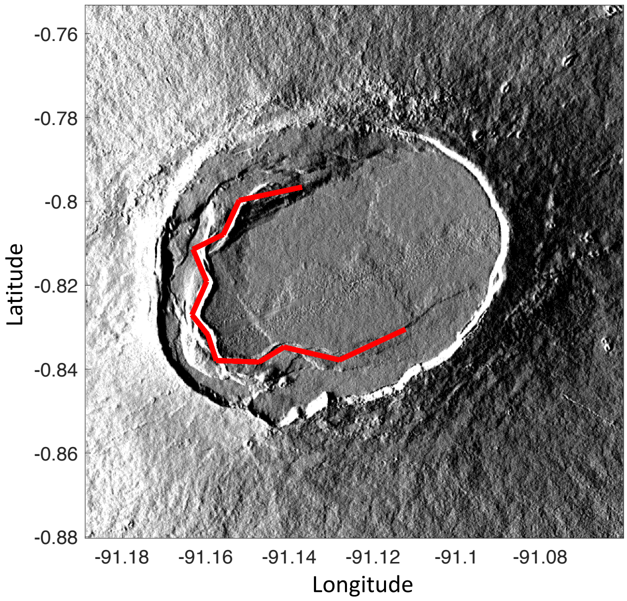

Figure 1. Shaded relief map of the Sierra Negra Volcano showing the intra-caldera fault system (thick red lines).

We assume that the sill surfaces are uniformly pressurized with no shear traction, consistent with the assumption of nearly static fluid. We use the Displacement Discontinuity Method (DDM) to model a crack-like sill. The boundary conditions on the sill are specified by

$$\underline{\sigma} = H\underline{\delta} + H_1\underline{s} = -\Delta p\underline{1} \tag{1a}$$

$$\underline{\tau_x} = J_{1x}\underline{s} + J_{2x}\underline{\delta}_x + J_{3x}\underline{\delta}_y = \underline{0} \tag{1b}$$

$$\underline{\tau_y} = J_{1y}\underline{s} + J_{2y}\underline{\delta}_x + J_{3y}\underline{\delta}_y = \underline{0} \tag{1c}$$

where $\underline{\sigma}$, $\underline{\tau_x}$ and $\underline{\tau_y}$ are the normal and horizontal shear tractions in the x and y directions on the sill surface, respectively. $\underline{\delta}$ is the opening of the sill, $\underline{s}$ is a vector of fault slips, and $\underline{\delta}_x$ and $\underline{\delta}_y$ represent shear displacement discontinuities (dislocations) of the sill in the x and y directions. Δp represents perturbation of pressure on the walls of the magma chamber associated with trapdoor faulting, and $\underline{1}$ is a vector of ones. Matrices H and H_1 map displacements into normal stress and matrices J_{ix}, $J_{iy}, i = 1, 2, 3$ map displacements into shear stress; all are computed using results for rectangular and triangular dislocations in a homogeneous elastic half-space (Okada, 1992; Maerten et al., 2005).

Kinematic conditions link the slip at the bottom of the fault to openings at the edge of the sill adjacent to the fault,

$$N_z B \underline{s} = E \underline{\delta} \tag{2a}$$

$$N_x B \underline{s} = E \underline{\delta}_x \tag{2b}$$

$$N_y B \underline{s} = E \underline{\delta}_y \tag{2c}$$

where B and E are matrices that extract elements associated with the bottom of the fault and the edge of the sill, respectively. N_z, N_x and N_y are matrices that extract vertical, east-west, and north-south components of displacements at the bottom of the fault.

The volume change of the magma chamber during a faulting event is found by integrating the opening, $\underline{\delta}$, over the surface of the sill, which can be written compactly as

$$\Delta V = \Psi \Delta p + \Phi \cdot \underline{s} \tag{3}$$

where $\Psi = (dV/dp)_s$ is the volume change per unit pressure change with no slip on the fault and $\Phi \cdot \underline{1}$ is the volume change for unit slip at constant pressure. Ψ is related to the chamber compressibility, $\beta_c = (1/V)\ (dV/dp) = \Psi/V$. Derivations of Ψ and Φ are given in Supplementary Materials. The first term of Eqn. [3] represents chamber volume change related to stress perturbation caused by trapdoor faulting. The second term gives the direct volume change caused by forced opening at the edge of the sill due to trapdoor faulting.

Since the trapdoor faulting event took place over a few seconds, negligible magma could have entered or exited the chamber. A linearized description of the mass change gives

$$\Delta m/\rho = V \beta_m \Delta p + \Delta V = 0 \tag{4}$$

where ρ and β_m are the magma density and compressibility, respectively.

Equations of mass conservation [4] and elasticity [3] provide two independent relations between volume and pressure changes during the faulting event. Combining them yields

$$\Delta p = \frac{-\Phi \cdot \underline{s}}{V\beta_m + \Psi}, \tag{5a}$$

$$\Delta V = \frac{V\beta_m (\Phi \cdot \underline{s})}{V\beta_m + \Psi}. \tag{5b}$$

Note that in the limit of small chamber volume and/or incompressible magma, $V\beta_m \to 0$, that $\Delta V \to 0$, while $\Delta p \to -\Phi \cdot \underline{s}/\Psi$. On the other hand in the limit of large volume and/or very compressible magma, $V\beta_m \to \infty$, that $\Delta p \to 0$ and $\Delta V \to \Phi\underline{s}$. This shows that the volume change of the magma chamber, which can be detected geodetically, is sensitive to the absolute chamber volume and the magma compressibility. Rewriting equation [5a],

$$V = -\frac{1}{\beta_m}\left(\Psi + \frac{\Phi \cdot \underline{s}}{\Delta p}\right). \tag{6}$$

Note that $\Delta p \leq 0$ (from 5a) and the term in parentheses in [6] is negative, such that $V > 0$.

The surface displacements $\underline{u}$ resulting from the fault-chamber interaction can also be expressed in terms of a vector of slips along the trapdoor fault $\underline{s}$, and a scalar pressure change in the magma chamber Δp,

$$\underline{u} = G_p\Delta p + G_s\underline{s}, \tag{7}$$

where G_p and G_s are computed from rectangular and triangular elastic dislocations. Estimates of Δp and $\underline{s}$ from geodetic measurements, obtained by inverting equation [7], can be used in equation [6] together with Ψ and Φ, which are determined by elasticity calculations given the fault and chamber geometry (Eqn.[4] and [5] in Supplementary Material). Thus, with bounds on β_m we can bound the absolute magma chamber volume V.

3 Results

We use GPS and InSAR data (from Jónsson (2009)) to estimate the fault slip (assuming pure dip-slip) and pressure change in the magma chamber using Eqn. [7]. The InSAR data has been corrected for inflation during the time span of the SAR acquisitions, both before and after the trap-door faulting. To avoid over-fitting, we smooth the solution by minimizing the second derivative of the fault slip. Specifically we minimize the objective function:

$$\begin{aligned} F(\Delta p, \underline{s}) =&(\underline{u}_{insar} - \underline{\hat{u}}_{insar})^T\Sigma_{insar}^{-1}(\underline{u}_{insar} - \underline{\hat{u}}_{insar}) \\ &+ w^2(\underline{u}_{gps} - \underline{\hat{u}}_{gps})^T\Sigma_{gps}^{-1}(\underline{u}_{gps} - \underline{\hat{u}}_{gps}) + \alpha^2||L\underline{\hat{s}}||_2^2, \end{aligned} \tag{8}$$

where $\underline{\hat{u}}$ is the predicted data, L is the second derivative operator, Σ_{insar} and Σ_{gps} are covariance matrices of InSAR and GPS data, respectively. We use data from the non-deforming areas north of the caldera to construct an empirical isotropic covariance matrix Σ_{insar} (Fig.S1). Correlation between GPS measurements are assumed to only exist between horizontal components. The choice of the smoothness parameter α^2 is based on an "L-curve" (Fig. S2). We weight the GPS data by w^2 to account for the disparity between the number of GPS data points and the number of InSAR data points. We chose a weight factor of $w = 5$ so that fits to both GPS and InSAR data are satisfactory (Fig. S3). We assume a shear modulus of $\mu = 10$ GPa and Poisson's ratio $v = 0.25$.

Previous inversions have well constrained the location and the shape of the chamber during inflationary episodes. We fix the sill geometry as described in S. Yun et al. (2006). To determine the fault dip, we tested a range of dips from outward dipping 70° to inward dipping 70°, constraining the bottom edge of the fault to be aligned with the edge of the sill. The misfit as a function of dip (Fig. 2a) is discontinuous because varying the dip changes the projection of the surface expression of the fault. We find that inward (northward) dips of 80 to 90° provide reasonable fits to both InSAR and GPS data, with a near-vertical, 88° dip being optimal. In contrast, Chadwick et al. (2006) and Jónsson (2009) concluded the best-fitting faults are more shallowly inward dipping (71°), although their calculations use a single planar fault and do not account for the presence of the magma chamber. We thus set the fault north dipping at 88° and only allow dip-slip on the fault. Fig. 2b shows the estimated fault slip and the amount of sill opening or closing. Note that the northern edge of the sill, opposite from the sector of the fault with maximum slip, is predicted to have closed. The estimated pressure change in the chamber is -0.8 MPa.

Fig. 3 shows the observed and predicted InSAR and GPS displacements. The preferred model can match both GPS and InSAR data quite well. In particular, the model accounts for the modest subsidence observed at the north edge of the caldera – opposite from the fault segment that experienced the most slip. Previous studies could not capture the observed subsidence with a model restricted to fault slip and not including the magma reservoir (Chadwick et al., 2006; Jónsson, 2009). In addition, our model cab explain most of the horizontal displacements recorded in the GPS data without requiring strike-slip motion on the trapdoor fault.

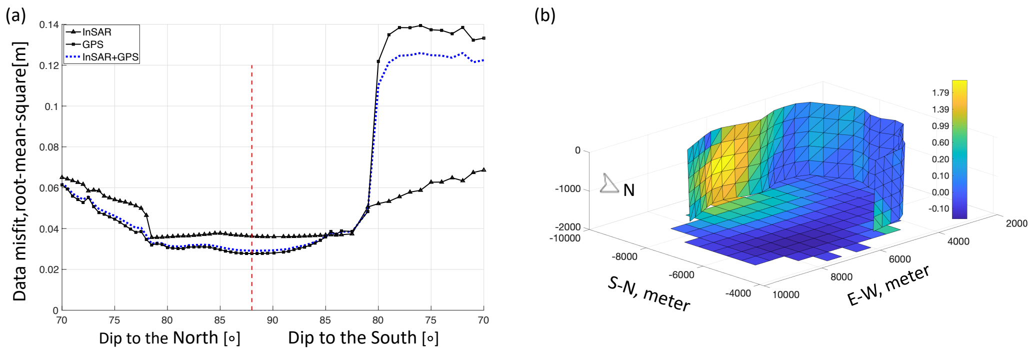

Figure 2. (a) Misfits of GPS (circles), InSAR (triangles) and their weighted combination (blue dotted line) as a function of fault dip. The vertical red line shows the optimal fault dip. (b) Estimated fault slip distribution and sill openings in meters with a fault dip of 88° to the North. Only dip slip is allowed on the fault.

4 Discussion

4.1 Upper Bound on Volume

The product $V\beta_m$ is estimated to be 1.7 m^3/Pa. In comparison, Anderson et al. (2019) estimate this product to be 1.3 - 5.5 m^3/Pa (95% bounds) from deformation and lava lake drainage during the early phase of the 2018 Kīlauea eruption. Segall and Anderson (2021) model episodic caldera collapse during the caldera forming phase of the 2018 eruption and find a range of 1.4 - 4.1 m^3/Pa. The estimate for Sierra Negra falls at the lower end of the range for Kīlauea.

Sierra Negra lavas are tholeiitic basalts. For bubble-free free basalt, which represents a lower bound on the compressibility, experimental results of Murase and McBirney (1973) yield $\beta_m \approx 10^{-10}$ Pa^{-1}. The thermodynamic model MELTS (Gualda et al., 2012; Ghiorso & Gualda, 2015) yields $\beta_m \approx 5.6\times10^{-11}$ Pa^{-1} for bubble-free basalt of Sierra Negra composition, roughly a factor of two less than the experimental value. Unless noted, we refer to the experimental value but acknowledge a factor of two uncertainty in this parameter. With the bubble-free experimental value of magma compressibility β_m, we obtain an upper bound on the absolute chamber volume of $V \sim 17.4$ km^3, corresponding to a maximum sill thickness of ~ 623 m, given the areal extent of the sill.

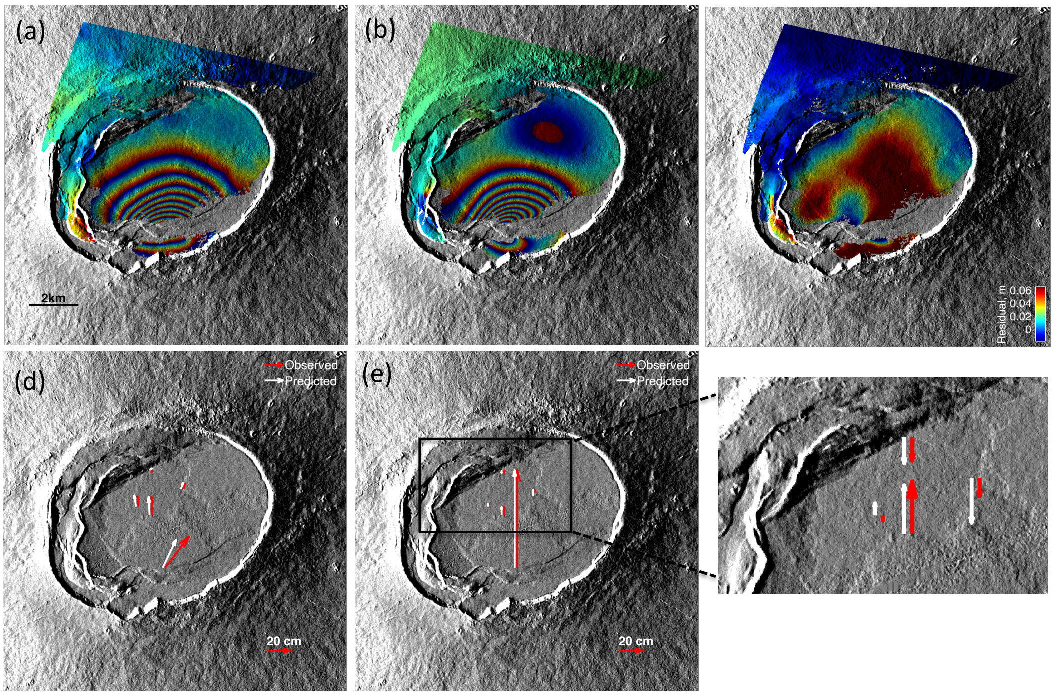

Figure 3. (a) Observed and (b) predicted InSAR data from the trapdoor-chamber model shown in Fig. 2(b), re-wrapped at 10 cm fringes. (c) Residuals between observed and predicted InSAR data. (d) Observed and predicted GPS horizontal displacements. (e) Observed and predicted GPS vertical displacements. The inset shows subsidence of the northernmost stations.

Given the high InSAR and GPS measurements quality, uncertainties in chamber volume V (Eq.[6]) mainly stem from uncertainties in the adopted fault-chamber geometry, the choice of elastic constants, and estimates of magma compressibility. We address each of these factors in the following.

Inversions of data from previous inflationary episodes have shown that Sierra Negra has a sill-like chamber (S. Yun et al., 2006; Amelung et al., 2000). However, geodetic data is not sensitive to the shape of the chamber as long as the chamber has a flat top. Estimation of the chamber volume V depends on the parameter Ψ, which describes the compressibility of the chamber and is determined by elasticity calculations given the chamber geometry. Perhaps unintuitively, the thickness of the sill has a limited impact on Ψ; The same is not true for β_c. For a penny-shaped sill at 2 km depth with radius a = 3 km in an elastic half-space with μ = 10 GPa, we compute Ψ = 9.1 m^3/Pa. In contrast, for a spherical chamber with radius small compared to its depth (the Mogi model)

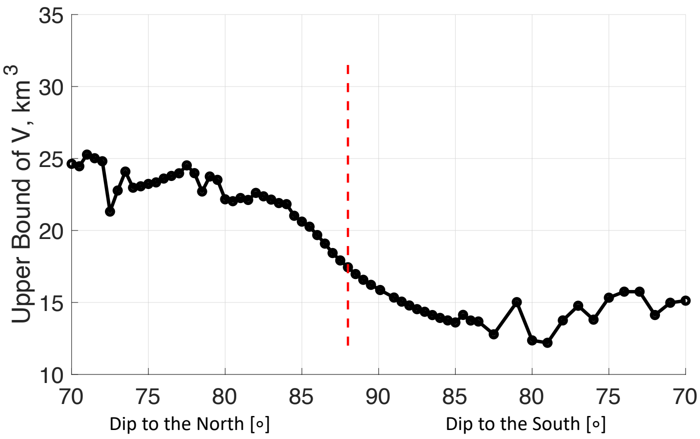

Figure 4. Estimated upper bound of chamber volume as a function of fault dip, assuming a magma compressibility of 10^{-10} Pa^{-1}. The red dashed vertical line indicates the optimal fault dip.

$\Psi \equiv dV/dP = \pi a^3/\mu$. With the same values of a and μ, $\Psi = 8.48$ m^3/Pa, a difference of only 6%.

Estimation of $\Phi{\cdot}\underline{s}/\Delta p$, and therefore the estimated reservoir volume, depends on fault dip. Fig. 4 illustrates how the estimated upper bound on volume varies with fault dip. Varying the fault dip from 85° S to 85° N, the estimated upper bound of chamber volume ranges from 13.6 km^3 to 20.6 km^3. Over this same range of dips, the estimated pressure change within the magma chamber due to trapdoor faulting ranges from -0.81 MPa to -0.93 MPa. The relatively small pressure drop on the chamber is consistent with the observation that the trapdoor faulting event did not significantly perturb the inflation rate (Chadwick et al. (2006), Fig.1D). If the pressure drop had been larger, we might have expected an increase in the inflation rate relative to the pre-faulting rate. The trapdoor faulting event before the 2018 eruption similarly does not significantly impact the uplift rate (Bell et al., 2021).

4.2 Lower Bound on Volume

An upper bound on magma compressibility, and hence a lower bound on chamber volume, is obtained by determining the maximum plausible exsolved CO_2 and H_2O volume fraction within the chamber. Following previous studies (Gerlach & Graeber, 1985;

Parfitt et al., 1995; Wasser et al., 2021), we use two sets of observations: melt inclusions and observed eruption fountain heights.

Koleszar et al. (2009) analyze olivine melt inclusions from Fernandina lavas similar to those at Sierra Negra. The most volatile-enriched melt inclusions, which are assumed to be representative of primitive mantle-derived magmas, contain up to 6000 ppm CO_2 and 1.1 wt. % H_2O. More typical samples, assumed to be representative of magma during crustal storage, contain 200 to 600 ppm CO_2 and 0.5 to 1.1 wt. % H_2O. Peterson et al. (2017) provide compositions for submarine glasses similar in composition and proximity to Sierra Negra with volatile contents ranging from 20 to 188 ppm CO_2 and 0.49 to 1.15 wt. percent H_2O. These glasses come from lavas that erupted on the sea floor and are thought to be continuously re-equilibrated during ascent.

We use the equilibrate function of MELTS (Gualda et al., 2012; Ghiorso & Gualda, 2015) on a typical Sierra Negra composition from Peterson et al. (2017) with the maximum observed CO_2 content of 6000 ppm from Koleszar et al. (2009), at pressure and temperature conditions for a chamber 2 km deep. The resulting magma compressibility is $\sim 1.5 \times 10^{-9}$ Pa^{-1} (Figure 5B), a 15 fold increase in β_m relative to bubble-free melt. This is an extreme bound on compressibility since some loss of CO_2 from the chamber is certain between eruptions. Taking ~600 ppm CO_2 as a more plausible upper bound on CO_2 content within the chamber results in a compressibility of $\sim 1.3{\times}10^{-10}$ Pa^{-1}, a 1.3 fold increase in β_m relative to the bubble-free melt.

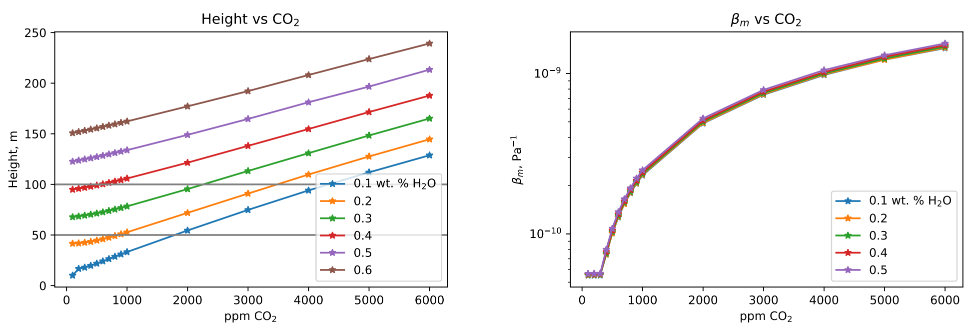

Figure 5. Dependence of fountain height on volatile content. A) Fountain height as a function of CO_2 content, for various water contents. Horizontal lines mark fountain height of 50 and 100 m. The volume flux is constrained to 100 m^3/s. B) Magma compressibility β_m as a function of CO_2 content, for various water contents.

The second approach uses an eruption conduit model to relate volatile content to observed lava-fountain height during the 2005 Sierra Negra eruption that followed a trap-door faulting event. D. J. Geist et al. (2008a) report fountain heights of up to 300 m on the second day of the eruption. Days 3-6 saw two primary fountains with heights of 30 m and 50 m. On day 7 a single fountain was observed with a height of 50 m. The estimated volume flux at this time was ~ 100 m^3/s from a 6-8 m diameter vent (D. J. Geist et al., 2008a). D. J. Geist et al. (2008a) employ the Head and Wilson (1987) single vapor phase model to estimate the volatile content and vent diameter on day 7 to be 0.1 to 0.2 weight % water.

We extend this approach to include both H_2O and CO_2. Specifically, our model assumes a cylindrical conduit, laminar flow up to the magma fragmentation threshold, fixed inlet pressure, and equilibrium H_2O and CO_2 degassing for a Sierra Negra composition derived from MELTS (Gualda et al., 2012; Ghiorso & Gualda, 2015). (Model details and code verification tests are given in the Supplemental Material.)

Parfitt et al. (1995) note that lava ponding, drain back, and bubble coalescence can all decrease the observed height relative to predictions from the Head and Wilson (1987) model. Figure 6A,B in Parfitt et al. (1995) shows that for a volume flux of 100 m^3/s, an eruption height of 50 m would be decreased by no more than 50% by these effects. So, we consider volatile compositions that would result in a fountain height of 100 m to account for these potential effects and obtain a maximum volatile composition.

Predicted fountain heights depend on both H_2O and CO_2 content, but because water is so much more soluble, the compressibility of magma in the chamber depends primarily on CO_2 content (Figure 5B). Thus, an upper bound on β_m is achieved with a lower value of water content (Figure 5A). A lower bound on water content from Koleszar et al. (2009) and Peterson et al. (2017) is 0.4 wt. %. From Figure 5A, a fountain height of 100 m is obtained with $\sim$600 ppm CO_2, which corresponds to a compressibility of $\sim 1.3 \times 10^{-10}$ Pa^{-1}. This is consistent with the estimate based on olivine melt inclusions.

Given that the MELTS-derived compressibility for bubble-free basalt is $5.6 \times 10^{-11} Pa^{-1}$, we suggest that a plausible lower bound on magma chamber volume is roughly a factor of two less than the upper bound. It should be noted, however, that the magma chamber may have been stratified with more gas rich magma toward the top. This could help explain the higher fire fountains observed at the onset of the 2005 eruption.

Thermal considerations presumably also place a lower bound on the magma chamber volume: A very thin sill would likely freeze between recharge events. However, apparently continuous recharge complicates such an analysis, which we defer to future studies.

4.3 An Estimate From Erupted Volume

From the product $V\beta_m$, we can obtain an estimation of the magma-chamber compressibility ratio $\eta \equiv \beta_m/\beta_c = V\beta_m/\Psi$. With a fault dip of 88°N we find $\eta \simeq 0.25$. Alternatively, η can be estimated from the ratio of the erupted volume to the geodetically-inferred chamber volume change during the eruption: $\eta = \Delta V_{erupt}/\Delta V - 1$ (Segall, 2010). S.-H. Yun (2007) estimates the volume change for the 2005 eruption ΔV to be 0.124 km^3 and the volume of lava that flowed into the caldera ΔV_{erupt} to be 0.141 km^3. D. J. Geist et al. (2008b), includes lava outside the caldera and estimates $\Delta V_{erupt} = 0.15$ km^3. Taking the larger value we find $\eta \simeq 0.21$, 16% smaller than the estimate based on trapdoor faulting. This change in η reduces the upper bound on chamber volume from 17.4 to 14.6 km^3, for the best-fitting fault dip. Note that this approach provides an independent estimate of the chamber volume as it does not require trapdoor faulting, but simply the erupted and geodetic volume change, as well as magma compressibility.

Finally, it should be noted that while η is a dimensionless parameter, Ψ is inversely proportional to the shear modulus μ. As a result, the estimation of V ($V = \eta\Psi/\beta_m$) is also inversely proportional to μ.

4.4 Relation to Other Volume Estimates

Body wave tomographic models beneath the Sierra Negra caldera have poor resolution in the shallow crust (less than 3 km depth) and therefore cannot resolve the magma chamber (Tepp et al., 2014). The 3D attenuation model identifies a shallow magma body between 0.5 km to 3 km below sea-level (Rodd et al., 2016), which is not inconsistent with our estimate of 623 meter sill thickness.

5 Conclusions

We have placed bounds on the total volume of the Sierra Negra volcano in the Galapagos by modeling the fault-chamber interaction during the trap-door faulting event on April 16, 2005. Our main findings are:

1. The best-fitting faults are near vertical and dip steeply to the north, 88°.
2. An upper bound on chamber volume is between 13.6 km^3 and 20.6 km^3, depending on fault dip. For the best fitting dip the volume is 17.4 km^3. (These estimates are for a shear modulus of 10 MPa; V is inversely proportional μ.)
3. The lower bound on volume is roughly one-half the upper bound.
4. These estimates are consistent with those obtained from the ratio of the erupted volume to geodetically determined change in magma chamber volume.

Acknowledgments

The research was supported by grants from the National Science Foundation Division of Earth Science (EAR-1829763). The InSAR and GPS data used can be downloaded from https://doi.org/10.5281/zenodo.5225160. The authors would like to thank helpful discussions with Dennis Geist, Mike Stock, and others.

References

Amelung, F., Jonsson, S., Zebker, H., & Segall, P. (2000, 10 26). Widespread uplift and /'trapdoor/' faulting on galapagos volcanoes observed with radar interferometry. *Nature*, *407*(6807), 993–996. Retrieved from `http://dx.doi.org/10.1038/35039604`

Anderson, K. R., Johanson, I. A., Patrick, M. R., Gu, M., Segall, P., Poland, M. P., ... Miklius, A. (2019). Magma reservoir failure and the onset of caldera collapse at kīlauea volcano in 2018. *Science*, *366*(6470).

Anderson, K. R., Poland, M. P., Johnson, J. H., & Miklius, A. (2015). Episodic deflation-inflation events at kīlauea volcano and implications for the shallow magma system. *Hawaiian Volcanoes: From Source to Surface*, *208*, 229.

Bell, A. F., La Femina, P. C., Ruiz, M., Amelung, F., Bagnardi, M., Bean, C. J., ... others (2021). Caldera resurgence during the 2018 eruption of sierra negra volcano, galápagos islands. *Nature communications*, *12*(1), 1–9.

Chadwick, W. W., Geist, D. J., Jónsson, S., Poland, M., Johnson, D. J., & Meertens, C. M. (2006). A volcano bursting at the seams: inflation, faulting, and eruption at sierra negra volcano, galápagos. *Geology*, *34*(12), 1025–1028.

Denlinger, R. P. (1997). A dynamic balance between magma supply and eruption rate at kilauea volcano, hawaii. *Journal of Geophysical Research: Solid Earth*, *102*(B8), 18091–18100.

Geist, D., White, W. M., Albarede, F., Harpp, K., Reynolds, R., Blichert-Toft, J., & Kurz, M. D. (2002). Volcanic evolution in the galápagos: The dissected shield of volcan ecuador. *Geochemistry, Geophysics, Geosystems*, *3*(10), 1–of.

Geist, D. J., Harpp, K. S., Naumann, T. R., Poland, M., Chadwick, W. W., Hall, M., & Rader, E. (2008a). The 2005 eruption of Sierra Negra volcano, Galápagos, Ecuador. *Bulletin of Volcanology*, *70*(6), 655–673. doi: 10.1007/s00445-007-0160-3

Geist, D. J., Harpp, K. S., Naumann, T. R., Poland, M., Chadwick, W. W., Hall, M., & Rader, E. (2008b). The 2005 eruption of sierra negra volcano, galápagos, ecuador. *Bulletin of Volcanology*, *70*(6), 655–673.

Gerlach, T. M., & Graeber, E. J. (1985). Volatile budget of Kilauea volcano. *Nature*, *313*(6000), 273–277. doi: 10.1038/313273a0

Ghiorso, M. S., & Gualda, G. A. (2015). An H2O–CO2 mixed fluid saturation model compatible with rhyolite-MELTS. *Contributions to Mineralogy and Petrology*, *169*(6), 1–30. doi: 10.1007/s00410-015-1141-8

Gualda, G. A., Ghiorso, M. S., Lemons, R. V., & Carley, T. L. (2012). Rhyolite-MELTS: A modified calibration of MELTS optimized for silica-rich, fluid-bearing magmatic systems. *Journal of Petrology*, *53*(5), 875–890. doi: 10.1093/petrology/egr080

Head, J. W., & Wilson, L. (1987). Lava fountain heights at pu'u '0'o, Kilauea, Hawaii. *Journal of Geophysical Research*, *92*(B13), 13715–13719. doi: doi:10.1029/JB092iB13p13715

Johnson, D. J. (1992). Dynamics of magma storage in the summit reservoir of kilauea volcano, hawaii. *Journal of Geophysical Research: Solid Earth*, *97*(B2), 1807–1820.

Jónsson, S. (2009, 6 9). Stress interaction between magma accumulation and trapdoor faulting on sierra negra volcano, galápagos. *Tectonophysics*, *471*(1–2), 36–44. Retrieved from http://www.sciencedirect.com/science/article/pii/S0040195108003880 doi: http://dx.doi.org/10.1016/j.tecto.2008.08.005

Jónsson, S., Zebker, H., & Amelung, F. (2005, 6 15). On trapdoor faulting at sierra negra volcano, galápagos. *Journal of Volcanology and Geothermal Research*, *144* (1–4), 59–71. Retrieved from http://www.sciencedirect.com/science/article/pii/S0377027304004160 doi: http://dx.doi.org/10.1016/j.jvolgeores.2004.11.029

Koleszar, A. M., Saal, A. E., Hauri, E. H., Nagle, A. N., Liang, Y., & Kurz, M. D. (2009). The volatile contents of the Galapagos plume; evidence for H2O and F open system behavior in melt inclusions. *Earth and Planetary Science Letters*, *287* (3-4), 442–452. doi: 10.1016/j.epsl.2009.08.029

Lees, J. M. (2007). Seismic tomography of magmatic systems. *Journal of Volcanology and Geothermal Research*, *167* (1), 37-56. Retrieved from https://www.sciencedirect.com/science/article/pii/S0377027307001965 (Large Silicic Magma Systems) doi: https://doi.org/10.1016/j.jvolgeores.2007.06.008

Maerten, F., Resor, P., Pollard, D., & Maerten, L. (2005). Inverting for slip on three-dimensional fault surfaces using angular dislocations. *Bulletin of the Seismological Society of America*, *95* (5), 1654–1665.

Mogi, K. (1958). Relations between the eruptions of various volcanoes and the deformations of the ground surfaces around them. *Earthq Res Inst*, *36*, 99–134.

Murase, T., & McBirney, A. R. (1973). Properties of some common igneous rocks and their melts at high temperatures. *Geological Society of America Bulletin*, *84* (11), 3563–3592.

Okada, Y. (1992). Internal deformation due to shear and tensile faults in a half-space. *Bulletin of the seismological society of America*, *82* (2), 1018–1040.

Parfitt, E. A., Wilson, L., & Neal, C. A. (1995). Factors influencing the height of Hawaiian lava fountains: implications for the use of fountain height as an indicator of magma gas content. *Bulletin of Volcanology*, *57* (6), 440–450. doi: 10.1007/BF00300988

Paulatto, M., Annen, C., Henstock, T. J., Kiddle, E., Minshull, T. A., Sparks, R., & Voight, B. (2012). Magma chamber properties from integrated seismic tomography and thermal modeling at montserrat. *Geochemistry, Geophysics, Geosystems*, *13* (1).

Peterson, M. E., Saal, A. E., Kurz, M. D., Hauri, E. H., Blusztajn, J. S., Harpp, K. S., ... Geist, D. J. (2017). Submarine basaltic glasses from the Galapagos Archipelago: Determining the volatile budget of the mantle plume. *Journal of Petrology*, *58*(7), 1419–1450. doi: 10.1093/petrology/egx059

Pietruszka, A. J., & Garcia, M. O. (1999). The size and shape of kilauea volcano's summit magma storage reservoir: a geochemical probe. *Earth and Planetary Science Letters*, *167*(3-4), 311–320.

Rawlinson, N., Fichtner, A., Sambridge, M., & Young, M. K. (2014). Seismic tomography and the assessment of uncertainty. *Advances in geophysics*, *55*, 1–76.

Reynolds, R. W., Geist, D., & Kurz, M. D. (1995, 12). Physical volcanology and structural development of sierra negra volcano, isabela island, galápagos archipelago. *Geological Society of America Bulletin*, *107*(12), 1398–1410. Retrieved from `http://gsabulletin.gsapubs.org/content/107/12/1398.abstract`

Rodd, R. L., Lees, J. M., & Tepp, G. (2016). Three-dimensional attenuation model of sierra negra volcano, galápagos archipelago. *Geophysical Research Letters*, *43*(12), 6259–6266.

Segall, P. (2010). *Earthquake and volcano deformation*. Princeton University Press.

Segall, P. (2013). Volcano deformation and eruption forecasting. *Geological Society, London, Special Publications*, *380*(1), 85–106.

Segall, P., & Anderson, K. (2021). Repeating caldera collapse events constrain fault friction at the kilometer scale. *Proceedings of the National Academy of Sciences*, *118*(30).

Segall, P., Cervelli, P., Owen, S., Lisowski, M., & Miklius, A. (2001). Constraints on dike propagation from continuous gps measurements. *Journal of Geophysical Research: Solid Earth*, *106*(B9), 19301–19317.

Tepp, G., Ebinger, C. J., Ruiz, M., & Belachew, M. (2014). Imaging rapidly deforming ocean island volcanoes in the western galápagos archipelago, ecuador. *Journal of Geophysical Research: Solid Earth*, *119*(1), 442–463.

Vasconez, F. J., Ramón, P., Hernandez, S., Hidalgo, S., Bernard, B., Ruiz, M., ... Ruiz, G. (2018). The different characteristics of the recent eruptions of fernandina and sierra negra volcanoes (galápagos, ecuador). *Volcanica*, *1*(2), 127–133.

Wasser, V. K., Lopez, T. M., Anderson, K. R., Izbekov, P. E., & Freymueller, J. T. (2021). Multidisciplinary Constraints on Magma Compressibility, the Pre-Eruptive Exsolved Volatile Fraction, and the H 2 O/CO 2 Molar Ratio for the 2006 Augustine Eruption, Alaska . *Geochemistry, Geophysics, Geosystems*, *22*(9), 1–24. doi: 10.1029/2021gc009911

Yamakawa, N. (1955). On the strain produced in a semi-infinite elastic solid by an interior source of stress. *J. Seismol. Soc. Japan, Ser. 2*, *8*(2), 84-98. Retrieved from https://ci.nii.ac.jp/naid/20001343438/en/

Yun, S., Segall, P., & Zebker, H. (2006, 2 1). Constraints on magma chamber geometry at sierra negra volcano, galápagos islands, based on insar observations. *Journal of Volcanology and Geothermal Research*, *150*(1–3), 232–243. Retrieved from http://www.sciencedirect.com/science/article/pii/S0377027305002611 doi: http://dx.doi.org/10.1016/j.jvolgeores.2005.07.009

Yun, S.-H. (2007). *A mechanical model of the large-deformation 2005 sierra negra volcanic eruption derived from insar measurements.* Stanford University.

Supporting Information for "Constraints on absolute chamber volume from geodetic measurements: Trapdoor faulting in the Galapagos"

Yujie Zheng[1], Laura Blackstone[2],Paul Segall[2]

[1]Division of Geological and Planetary Sciences, California Institute of Technology

[2]Geophysics Department, Stanford University

Contents of this file

References

Geist, D. J., Harpp, K. S., Naumann, T. R., Poland, M., Chadwick, W. W., Hall, M., & Rader, E. (2008). The 2005 eruption of Sierra Negra volcano, Galápagos, Ecuador. *Bulletin of Volcanology*, *70*(6), 655–673. doi: 10.1007/s00445-007-0160-3

Mastin, L. (1995). A numerical program for steady-state flow of Hawaiian magma-gas mixtures through vertical eruption conduits. *U. S. Geol. Surv. Open-File Report*, *pp*, 95–756.

Peterson, M. E., Saal, A. E., Kurz, M. D., Hauri, E. H., Blusztajn, J. S., Harpp, K. S., ... Geist, D. J. (2017). Submarine basaltic glasses from the Galapagos Archipelago: Determining the volatile budget of the mantle plume. *Journal of Petrology*, *58*(7), 1419–1450. doi: 10.1093/petrology/egx059

1. Derivations

Combining Eqn. [1b], [1c], [2b] and [2c], we can relate shear displacements $[\underline{\delta}_x; \underline{\delta}_y]$ to slips on the fault

$$\begin{bmatrix} \underline{\delta_x} \\ \underline{\delta_y} \end{bmatrix} = \begin{bmatrix} -J_{2x} & -J_{3x} \\ -J_{2y} & -J_{3y} \\ E & 0 \\ 0 & E \end{bmatrix}^{-1} \begin{bmatrix} J_{1x} \\ J_{1y} \\ N_x B \\ N_y B \end{bmatrix} \underline{s} \tag{1}$$

Combining Eqn. [1a] and [2a] and inverting yields the sill openings δ

$$\underline{\delta} = \begin{bmatrix} H \\ E \end{bmatrix}^{-1} \begin{bmatrix} -\Delta p \underline{1} - H_1 \underline{s} \\ N_z B \underline{s} \end{bmatrix} = \begin{bmatrix} Q_p & Q_f \end{bmatrix} \begin{bmatrix} -\Delta p \underline{1} - H_1 \underline{s} \\ N_z B \underline{s} \end{bmatrix} \tag{2}$$

where the latter form serves to define $[Q_p \;\; Q_f]$. The volume change of the sill can be computed by integrating the openings of the magma chamber:

$$\Delta V = \sum_i \delta_i dA_i = -\sum_i \left[dA_i \sum_j Q_{p_{ij}} \right] \Delta p + \sum_i \left[dA_i \sum_j [Q_f N_z B - Q_p H_1]_{ij} s_j \right] \tag{3}$$

where dA_i is the area of the i^{th} segment of the sill. Let

$$\Psi = -\sum_i \left[dA_i \sum_j Q_{p_{ij}} \right] \tag{4}$$

$$\Phi = \sum_i dA_i [Q_f N_z B - Q_p H_1]_{ij} \tag{5}$$

The surface measurements $\underline{u}$ resulting from the fault-chamber interaction can be described as

$$\underline{u} = G\underline{\delta} + G_1\underline{s} + G_2\underline{\delta_x} + G_3\underline{\delta_y} + \underline{\epsilon} \tag{6}$$

where G, G_1 G_2 and G_3 are Green's functions in the elastic half-space and $\underline{\epsilon}$ represents measurement errors. Replacing $\underline{\delta}$, $\underline{\delta_x}$ and $\underline{\delta_y}$ with Eqn. (2) and (1), we get

$$\begin{aligned} \underline{u} &= -GQ_p\underline{1}\Delta p + \left[G(Q_f N_z B - Q_p H_1) + G_1 + \begin{bmatrix} G_2 & G_3 \end{bmatrix} \begin{bmatrix} -J_{2x} & -J_{3x} \\ -J_{2y} & -J_{3y} \\ E & 0 \\ 0 & E \end{bmatrix}^{-1} \begin{bmatrix} J_{1x} \\ J_{1y} \\ N_x B \\ N_y B \end{bmatrix} \right] \underline{s} + \underline{\epsilon} \\ &= G_p \Delta p + G_s \underline{s} + \underline{\epsilon} \end{aligned} \tag{7}$$

The second equation serves to define the matrices G_p and G_s. Notice that the surface displacements are expressed in terms of a vector of fault slips along the trapdoor fault, and a scalar pressure change in the magma chamber.

2. Figures S1-S3

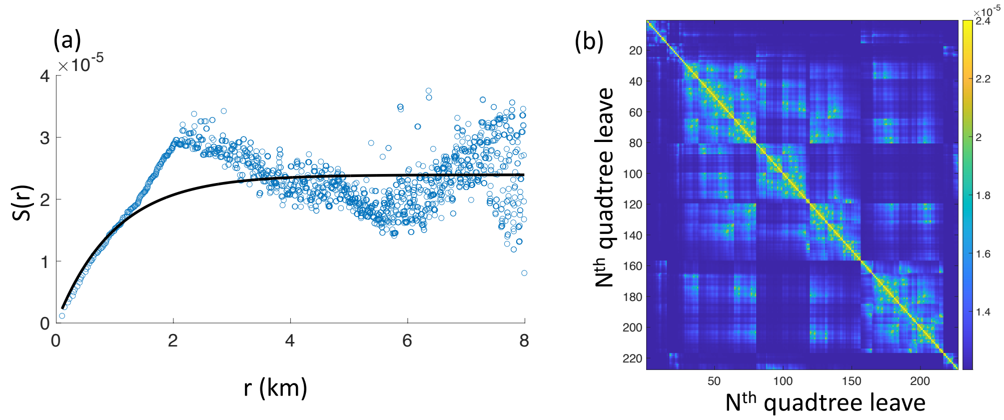

Figure S1. We use the non-deforming areas north of the caldera to estimate InSAR noise structure function and to derive an experimental covariance matrix. To reduce InSAR observations, we down-sample InSAR observations using a quadtree approach. (a) Structure function of InSAR noise. The black line is fit to the structure function. (b) Estimated covariance matrix for down-sampled InSAR quadtree leaves.

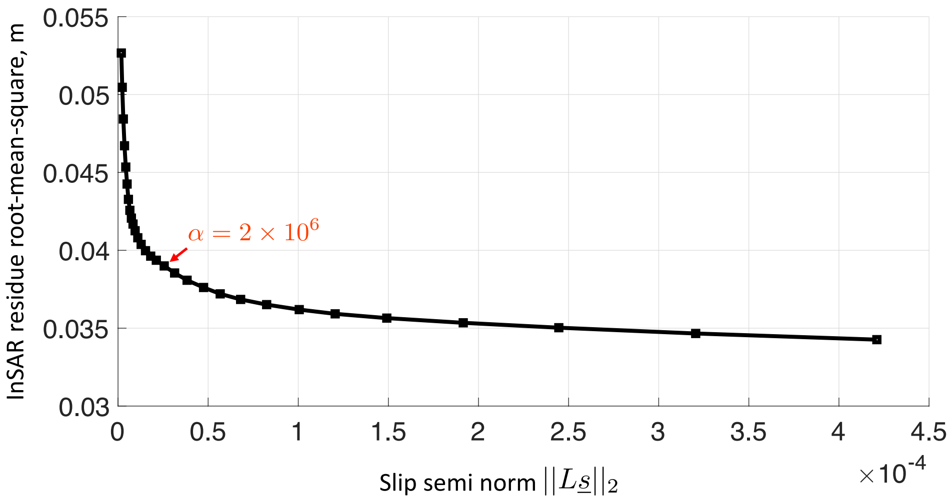

Figure S2. To determine the smoothness parameter, we fix the fault dip angle to be 88° northward and compute the L-curve with smoothness parameters varying from 10^5 to 10^8. The chosen smoothness parameter is marked by the red arrow.

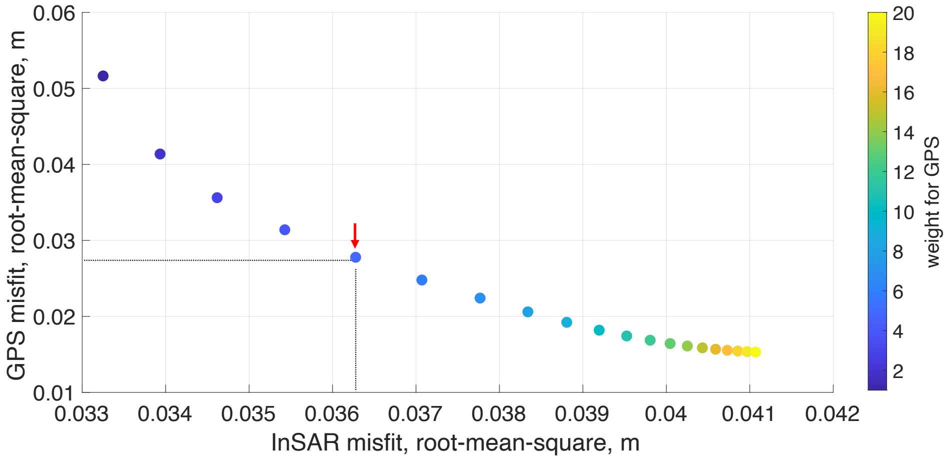

Figure S3. Data misfit as a function of weighting for GPS vs. InSAR data. We choose a weighting factor of 5 because it significantly reduces the misfit to the GPS data while not compromising goodness-of-fit for InSAR data too much.

3. Conduit Model

We assume a cylindrical conduit of constant radius r connecting the top of the magma reservoir to the surface. The governing equations are radially averaged to produce a one-dimensional, in depth, model. Flow below the fragmentation depth is laminar. The pressure at the base of the conduit is taken to be 54 MPa. Figure S4 shows a schematic of this model. The model does *not* allow for variations in conduit radius, relative motion of the bubble and liquid phases, the presence of a solid phase, or bubble-dependant viscosity.

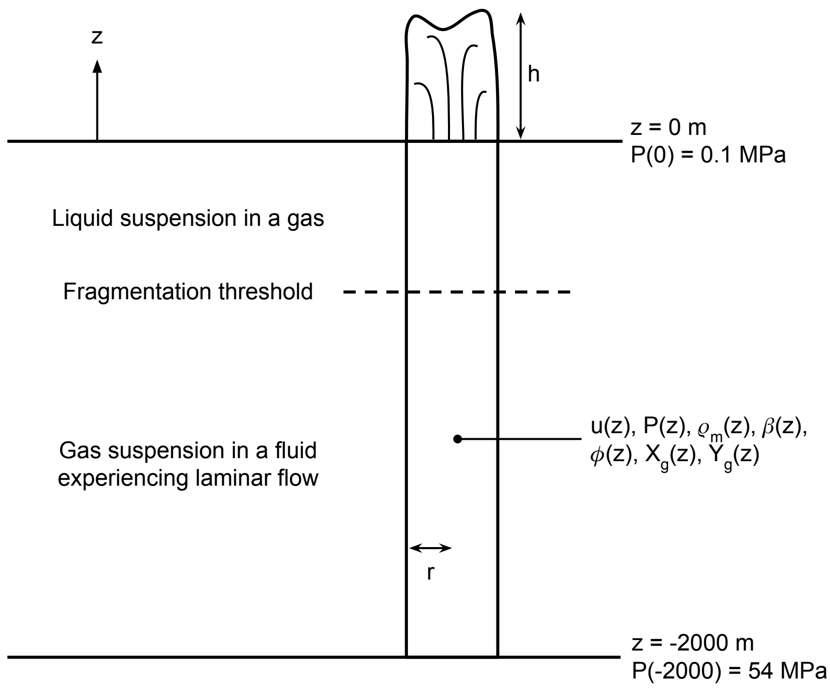

Figure S4. Schematic of conduit model showing radius r, fountain height h, mixture velocity u, pressure P, melt (liquid plus gas) density ρ_m, melt compressibility β_m, gas volume fraction ϕ, mass fraction of H_2O gas X_g, and mass fraction of CO_2 gas Y_g.

Magma in the conduit obeys conservation of mass and momentum. The former, $d(u\rho_m)/dz$, where u is the mixture velocity and ρ_m is density of the melt (liquid plus gas), can be recast as:

$$\frac{du}{dz} = -u\beta_m \frac{dP}{dz}[s^{-1}] \tag{8}$$

where P is pressure in Pa, z [m] is depth (positive in the up direction), β_m is the magma compressibility. Using this relationship, conservation of momentum can be written as

$$\frac{dP}{dz} = -\left(\rho_m g + 2\tau/r\right)\left(1 - u^2/c^2\right)^{-1}[Pa/m] \tag{9}$$

(Mastin, 1995), where $g = 9.81$ [m/s^2] is acceleration due to gravity, τ [N/m^2] is the wall shear stress, and $c = (\rho_m\beta_m)^{-1/2}$ [m/s] is the sound speed of the mixture.

The shear stress acting on the conduit wall is $\frac{1}{2}f_0\rho_m u^2$ [Pa] where f_0 is the Darcy-Weisbach friction factor, here assigned a value of 0.1. Shear stress due to laminar flow, below fragmentation, is $4\mu u/r$ [Pa], where μ is the magma viscosity. The total shear stress τ is thus:

$$\tau = \frac{1}{2}f_0\rho_m u^2 + 4\mu u/r[Pa] \textit{ below} \text{ fragmentation} \tag{10}$$

$$\tau = \frac{1}{2}f_0\rho_m u^2[Pa] \textit{ above} \text{ fragmentation} \tag{11}$$

Fragmentation occurs when the volume fraction of gas ϕ reaches 0.75.

To obtain equilibrium exsolution of H_2O and CO_2 we use the equilibrate function of MELTS applied to a typical Sierra Negra composition with varying volatile contents, at 1200°C, allowing only fluid and liquid phases. The composition used is sample D34a from (Peterson et al., 2017). The equilibrate function yields gas composition, liquid composition, melt density ρ_m, melt compressibility β_m, and gas volume fraction ϕ. To improve code efficiency, we create lookup tables relating the parameters of interest to $\log P$ for fixed total volatile content. Cubic spline interpolation is used to determine quantities at intermediate pressures. The model assumes equilibrium exsolution continues to occur following fragmentation.

Volume flux refers to the volume of liquid exiting the top of the conduit per second, $\pi r^2 u_{z=0}(1-\phi_{z=0})$ [m^3/s]. The height of the lava fountain is calculated using the ballistic equation, $h = \frac{1}{2} g u_{z=0}^2$ [m].

3.1. Solution method

For a given volatile content and conduit radius, the code uses the shooting method to adjust the velocity at the bottom of the conduit until the pressure at the top of the conduit matches atmospheric pressure conditions. If no such solution can be found then a choked boundary condition, having a Mach number $M \equiv c^2/u^2$ of exactly 1 at the surface, is attempted. To integrate the equations in z, our Python implementation uses scipy.integrate.solve_ivp() with backwards differentiation, a relative tolerance of 1×10^{-12}, and an absolute tolerance of 1×10^{-12}. The conduit radius was adjusted for each volatile composition until the volume flux was within ± 3 m^3/s of 100 m^3/s to match the observed value in Geist et al. (2008).

3.2. Validation

Output from this code in the case of zero CO_2 is validated against the single volatile phase (water) model from Mastin (1995). Settings and parameters used in the benchmark model include the default Kilauea basalt composition, only liquid and gas phases, fixed radius with depth, lithostatic pressure in the chamber, atmospheric surface pressure, fragmentation at a gas volume fraction of 75%, equilibrium exsolution allowed after fragmentation, conduit length of 2000 m, and fixed temperature of 1200°C. Radius was adjusted for each volatile composition to match a mass flux consistent with a 100 m^3/s volume flux. The output from the two models, shown in Figure S5, have reasonable agreement for all compositions considered.

Water (wt.%)	Benchmark fountain heights (m)	Calculated fountain height (m)	Deviation from benchmark
0.2	36	42	16.67%
0.3	78	68	-12.82%
0.4	107	95	-11.21%
0.5	139	123	-11.51%
0.6	173	151	-12.72%

Figure S5. Table comparing calculated fountain height for water-only compositions to output from Conflow (Mastin, 1995).